Nanoscale

Accepted Manuscript

This article can be cited before page numbers have been issued, to do this please use: V. Gómez-Vallejo, M. Puigivila, S. Plaza-García, B. Szczupak, R. Piñol, J. L. Pola, V. Sorribas, G. Lou, S. Veintemillas-Verdaguer, P. Ramos-Cabrer, J. Llop and A. Millán, *Nanoscale*, 2018, DOI: 10.1039/C8NR03084G.

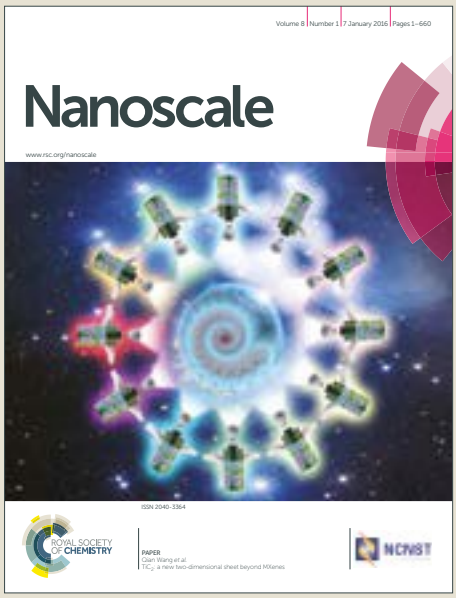

View Article Online
DOI: 10.1039/C8NR03084G

PEG-Copolymer-coated Iron Oxide Nanoparticles that Avoid the Reticuloendothelial System and Act as Kidney MRI Contrast Agents.

Vanessa Gómez-Vallejo[1], María Puigivila[2], Sandra Plaza-García[2], Boguslaw Szczupak[3], Rafael Piñol[4], José L. Murillo[4], Victor Sorribas[5], Gustavo Lou[4], Sabino Veintemillas[6], Pedro Ramos-Cabrer[2,7], Jordi Llop[1]*, Angel Millán[4]**

[1] Radiochemistry and Nuclear Imaging Group. CIC biomaGUNE, 20014 , Donostia-San Sebastián, Spain

[2] Magnetic Resonance Imaging Department. Molecular Imaging Unit, CIC biomaGUNE, 20014, Donostia-San Sebastián, Spain

[3] Department of Telecommunications and Teleinformatics. Wroclaw University of Science and Technology, Wybrzeze Wyspianskiego 27, 50-370 Wroclaw, Poland

[4] ICMA. CSIC-Universidad de Zaragoza, C/ Pedro Cerbuna 10, 50009 Zaragoza, Spain

[5] Departamento de Toxicología, Universidad de Zaragoza, 50013 Zaragoza. Spain

[6] ICMM. CSIC, Sor Juana Inés de la Cruz 3, Cantoblanco, 28049 Madrid, Spain.

[7] Ikerbasque, Basque Foundation for Science, 48013 Bilbao, Spain.

KEYWORDS: nanoparticles, biodistribution, RES, SPECT, MRI, PEG, iron oxide,

ABSTRACT

View Article Online
DOI: 10.1039/C8NR03084G

In vitro experiments have shown the great potential of magnetic nanocarriers for multimodal imaging diagnosis and non-invasive therapies. However, their extensive clinical application is still jeopardized by a fast retention in the reticuloendothelial system (RES). Other issue that restrains their potential performance is a slow degradation and excretion, which increases their toxicity risks. We report a promising case in which multicore iron oxide nanoparticles coated with poly(4-vinylpyridine) polyethylenglycol copolymer show low RES retention and high urinary excretion, as confirmed by Single Photon Emission Computerized Tomography (SPECT), Gamma Counting , Magnetic Resonance Imaging (MRI) and Electron Microscopy (EM) biodistribution studies. These iron oxide-copolymer nanoparticles have high PEG density in their coating that may be responsible for this effect. Moreover they show a clear negative contrast in MR imaging of kidneys. These nanoparticles with an average hydrodynamic diameter of approximately 20 nm, were nevertheless able to cross the glomerulus wall, which has an effective pore size of approximately 6 nm.,Transmission Electron Microscopy inspection of kidney tissue revealed the presence of iron containing nanoparticle clusters in proximal tubule cells. This therefore makes them exceptionally useful as magnetic nanocarriers and as a new MRI contrast agent for kidneys.

View Article Online
DOI: 10.1039/C8NR03084G

Introduction

In vitro experiments have shown the enormous potential of nanocarriers, in general, and of magnetic nanocarriers, in particular, in biomedical applications[1] Their capacity for targeted drug delivery, stimuli-responsive drug release, and multi-therapeutic loading are taking over traditional drug therapy. They have also shown considerable potential for multimodal imaging diagnosis[2] and non-invasive therapies, including localized externally-triggered hyperthermia and combined therapies.[3] However, translating all these benefits into real clinical practice has met a bottleneck: nanocarriers are tenaciously retained by the reticuloendothelial system (RES) before having the chance to hit the target. Apart from a severe drop in targeting efficiency, persistent retention in the liver delays clearance, increases toxicity, and restricts the use of nanocarriers as MRI contrast agents to this organ.

The recognition and uptake of nanoparticles (NPs) by the Kupfer cells of the immune system is highly dependent on the NP surface.[4,5] However, when nanoparticles encounter the macrophages, their surface is not the same as it originally was, given that it has already been covered with a corona of plasma proteins in blood. These proteins are the real triggering factor for uptake by macrophages. Furthermore, the composition and structure of this protein corona depends on the adsorption properties of the original nanoparticle surface, thereby indirectly determining the degree of NP retention by the RES. As such, the efficacy of poly(ethylene glycol) (PEG) coatings in preventing a reaction by the RES has already been clearly demonstrated[5]. And it has also been shown that the real effect by PEG coatings consists in promoting the adherence of clustering proteins,[6] which are not recognized by macrophages, as opposed to albumin, which is the usual component of the protein corona of NPs. As an example, the RES retention of phosphate-coated Au NPs (D_H = 11 nm) decreased from 93% ID to 3.3% after coating with 10

View Article Online
DOI: 10.1039/C8NR03084G

kD PEG.[7] It has also been shown that the effect by PEG depends on the density of PEG on the shell surface and in the chain size.[7]

The coating on the core-shell iron oxide nanoparticles (IONPs) used in this work has been designed to achieve a high PEG density. First, iron oxide nanoparticles are directly precipitated in a poly(4-vinyl pyridine) (P4VP) matrix and are redispersed in slightly acidic solutions. Subsequently, PEG acrylate chains are incorporated into the pyridine groups by a Michael reaction, with an acrylate terminal group at one of the ends of the PEG chain, as shown in **Scheme 1**, thereby providing the NPs with a high-density PEG coating of the NPs. By increasing the pH to blood level (7.4), the free pyridine groups are made hydrophobic. As it has been previously reported, this type of NP does not present either hematological complications[8] or relevant cell cytotoxicity.[9] Moreover, the synthetic strategy permits easy multifunctionalization, such as with optical dyes,[9] antibodies, therapeutic drugs, and molecular thermometers.[10]

Biodistribution techniques can be classified into two categories: *in vivo* instant imaging[11-14] and *ex vivo* postmortem analysis of extracted tissues.[15] In the case of iron oxide nanoparticles (IONPs), *ex vivo* chemical analysis is not highly reliable[16,17] due to the variable content of endogenous iron in tissues. However, IONPs can be detected and quantified *ex vivo* in a magnetometer,[18] and they can be imaged *in vivo* by MRI thanks to the intense negative contrast they provide due to changes in the water proton nuclear relaxation induced by superparamagnetic nanoparticles.[19] MRI has the advantage of being a non-invasive imaging technique that offers excellent soft tissue contrast, as well as better spatial resolution and prolonged observation time. However, the sensitivity of MRI is low compared to radiochemical methods. For instance, the in vivo MRI detection threshold of IONPs (approximately 200–700 mg (Fe) for a 70-kg patient) is 200 times greater than that of Positron Emission Tomography (PET).[20] Therefore, a convenient

View Article Online
DOI: 10.1039/C8NR03084G

way to follow the whole cycle of IONPs in the body would be to use a combination of both methods: a) radio imaging[21] to precisely screen the circulation of IONPs during the first critical hours (or few days) and b) MRI to check the persistence of IONPs in a certain organ or tissue. Alternatively, sensitivity and spatial resolution in *in vivo* magnetic nanoparticles (MNP) detection are greatly enhanced in magnetic particle imaging (MPI), which is based on a direct detection of the MNPs from their non-linear magnetization, although it is only applicable In NPs with a relatively large size.[22]

Positron or gamma-emitting radiolabels are probably the most direct and sensitive detection methods, with the highest penetration among imaging techniques.[23,24] However, in order to take full advantage of these benefits in IONP biodistribution studies, the radiolabels should form part of the nanoparticle structure so they unequivocally mark the NP position. Nevertheless, in most cases, radiotracers are introduced by adsorption on the IONP surface,[25] by chelation[26] or covalent bonding[20] to the polymer shell, or by encapsulation in a lipid membrane.[27] Then, the metabolic system can cause the radiolabels to detach from the nanoparticle,[28] thus falsifying the biodistribution pattern.[25,29-32] The most direct method for radiolabeling IONPs is through the transformation of some Fe atoms in the oxide structure into ^{59}Fe,[33] (a PET radiotracer), or by generating radioactive ^{13}N from ^{16}O by proton irradiation.[34] Recently, the radiotracer has been incorporated to the iron oxide nanoparticle at the synthesis stage.[35,36] Two different methods have been proposed: 1) thermal decomposition of $Fe(acac)_3$ in the presence of $^{111}InCl_3$[35] and 2) co-precipitation of Fe(III) and ^{68}Ga(III) chloride salts.[36] In the former case, the synthesis procedure is complex, given that it involves a reflux process at a high temperature. In the latter case, the drawback is the purification step after precipitation.

View Article Online
DOI: 10.1039/C8NR03084G

^{111}In is a commercially available radionuclide that, together with ^{99m}Tc, is used the most in clinical nuclear medicine.[26] Its half-life of 2.8 days makes it very adequate for NP biodistribution studies. However, the use of this radionuclide has been mostly related to purely organic NPs,[27,37-39] and rarely to core-shell inorganic NPs,[40] including iron oxides.[41] In this report, a direct and reliable method of gamma-radiolabeling of IONPs has been achieved by doping the crystalline structure with ^{111}In through simple coprecipitation in the presence of this ion. The biodistribution of the NPs in mice after coating with P4VP-APEG amphiphilic copolymer has been followed by SPECT, gamma-counting, and MRI.

Results and discussion

Direct labeling of iron oxide nanoparticles with gamma-emitter ^{111}In.

In order to determine the quality of the radiolabeling, the capacity of Fe^{3+} and In^{3+} to precipitate in the form of double oxides was evaluated by X-ray powder diffraction analysis of oxide precipitates from solutions of a mixture of Fe^{3+} and In^{3+} chloride salts. The diffraction patterns of precipitates from solutions containing an In^{3+} atomic ratio of 0.1 or less (Figure 1S) showed a single crystalline structure corresponding to g-Fe_2O_3 (maghemite), thereby indicating that In and Fe were coprecipitating in the same crystal lattice. Moreover, the diffraction peaks gradually shifted to lower angles as the In ratio in the solution was increased (inset in Figure 1S), which indicates an increase of the cell parameter due to the progressive incorporation of In^{3+} ions (with a higher ionic radius than Fe^{3+}) into the iron oxide lattice. When the In^{3+} ratio in the solution was increased to 0.5, the precipitate was also single phase (Figure 2S), but the structure was that of $In(OH)_3$, with a lower lattice parameter due to the replacement of In^{3+} ions by smaller Fe^{3+} ions. We could therefore state that under our precipitation conditions, In and Fe are apparently

View Article Online
DOI: 10.1039/C8NR03084G

interchangeable in their respective oxide structures, wherefore ^{111}In ions will detach from iron oxide NPs only when the whole nanoparticle is dissolved. Nevertheless, the possibility that In^{3+} might leach from the nanoparticles after injection in blood was tested by dialysis. An aqueous suspension of In/Fe oxide nanoparticles having the same In/Fe ratio as that which was used in the SPECT and gamma-counting experiments was dialysed against human serum for 24 hours. The analysis of the dialysate by atomic emission (ICP- OES) showed no presence of either Fe^{3+} or In^{3+} ions within the detection limits of the instrument.

NP size and structure.

The size characterization of NPs was performed using non-radioactive samples prepared under the same conditions as those used in the biodistribution studies. TEM images of the samples before PEG coating (Figure 1A) show non-aggregated spherical IONPs with an average size of 3.8±0.8 nm and a lognormal size distribution (Figure 1B). CryoTEM images of the NPs after PEG coating showed that the IONPs in suspension were grouped in a grape-like loosely packed clusters (Figure 1C). We calculated the diameter of spheres with the same volume estimated from cryoTEM images, and the average value (SD) was 11.5(5.9). The contrast between the polymer and the water background was too low to allow observation of the polymer coating around the iron oxide nuclei. Therefore, the total size of the core-shell nanoparticles was determined by DLS. This resulted in an average hydrodynamic diameter of 18 nm. The size distribution is shown in Figure 1D, and an overview of the synthesis procedure and the NP structure is presented in Scheme 1. The average sizes of the IONPs represent approximately 15-20% of the average hydrodynamic sizes. Considering that the pyridine groups are hydrophobic and that PEG residues are hydrophilic at the pH of the medium (7.40), we propose the following as a tentative description of the structure of the MNP@P4VP@APEG composite nanoparticles in

View Article Online
DOI: 10.1039/C8NR03084G

suspension: internally, they would be formed by a folded P4VP chains holding the MNPs in the interior by N-Fe coordination bonds, and externally, they would be formed by solvated PEG chains in a radial disposition. More information about the PEG coating reaction and the brush structure of the P4VP-APEG graft copolymer coating is given in the SI file. This brush structure confers a high PEG density to the coating, in comparison with linear polymer folded structure.

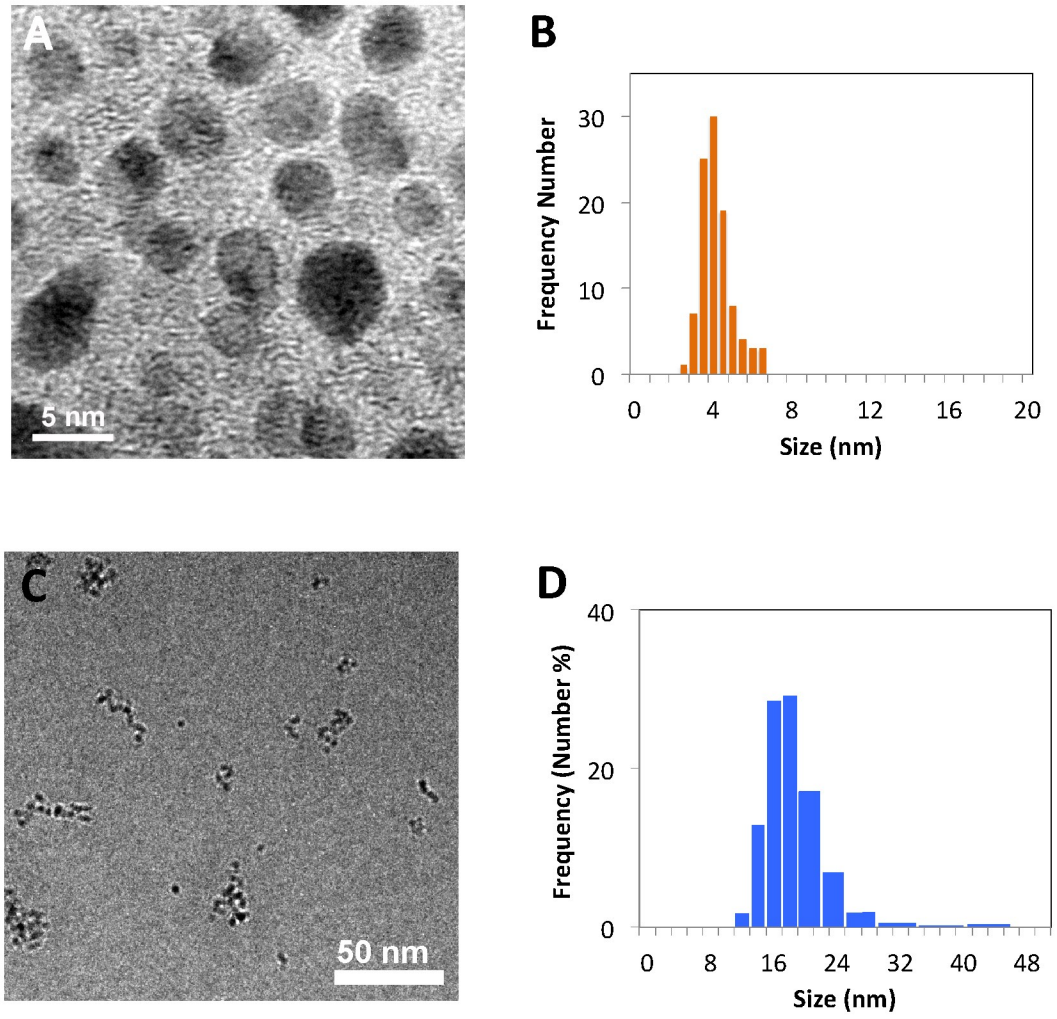

Figure 1. A) TEM image of iron oxide-P4VP nanoparticles suspended in water at pH = 3, before being coated with PEG; and B) Size distribution by number of iron oxide nanoparticles from TEM images. C) cryo TEM and STEM (inset) images of iron oxide@P4VP@APEG copolymer nanoparticles suspended in water at pH = 7.4; and D) size distribution in frequency by number (%) from DLS data.

View Article Online
DOI: 10.1039/C8NR03084G

Scheme 1. Simplistic diagram of the structure and synthesis of radiolabeled iron oxide-polymer nanoparticles showing: the position of the radionuclide, the grafting of APEG chains to pyridine moieties on P(4VP) polymer matrix, the amphiphilic character of the P4VP-APEG polymer shell, and the distribution of positive and negative charges in the core-shell nanoparticles. The spherical shape is a drawing license, and it does not correspond either to the real shape of the iron oxide clusters, which is grape-like (as it can be seen in Fig. 1), or to the shape of the polymer shell.

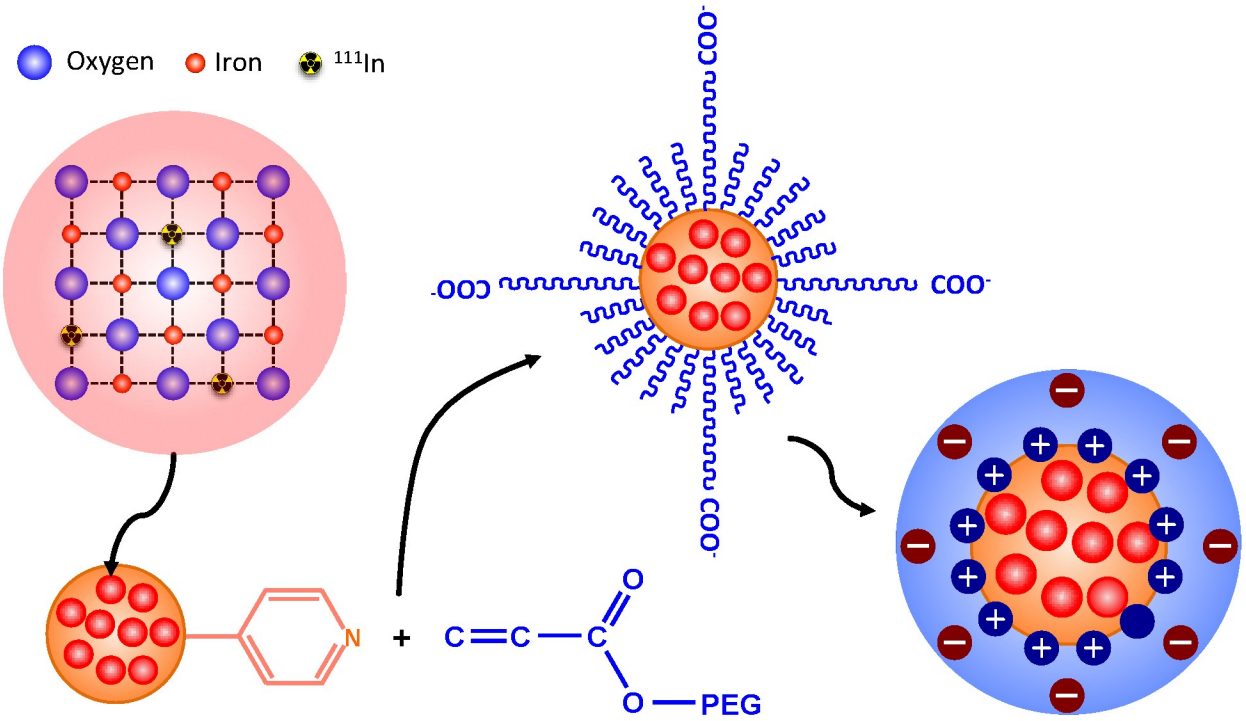

Radiotracing experiments.

The biodistribution of nanoparticles after tail injection of 150 µL of the suspension described in the experimental section was followed by SPECT (dose of 18 µmol Fe/kg). The images gave a very clear signal of the biodistribution of IONPs, even when the injected dose was less than the typical values used in MRI clinical studies[31] (40-70 µmol Fe/kg) and 3 times lower than the values at which clinical problems appear[42] (60 µmol Fe/kg). Figure 2 shows the maximum

View Article Online
DOI: 10.1039/C8NR03084G

intensity projections (MIPs). It can be clearly observed that the maximum activity in the first instance is detected in the blood and in organs with high blood irrigation such as the heart and lungs, but also in the liver, kidneys, etc. As time elapses, the activity in the blood and lungs decreases, while it increases in the bladder and kidneys. After 3.5 hours, all the activity is concentrated in the kidneys and, to a lesser extent, in the liver and bladder.

The accumulation of the ^{111}In-labelled iron oxide nanoparticles in several organs was also followed by radiocounting (Figure 3), which confirmed the SPECT observations. The presence in blood is very high during the first minutes and then decreases substantially after 15 min. Presence in the urine increases up to 30 min, and then it drops, probably due to the fact that the animals inevitably urinate. A certain amount of activity is also found in the spleen, which could not be detected clearly in the SPECT images. After the first hour and over the next 24 hours, the activity in the kidney, liver, and spleen decreases.

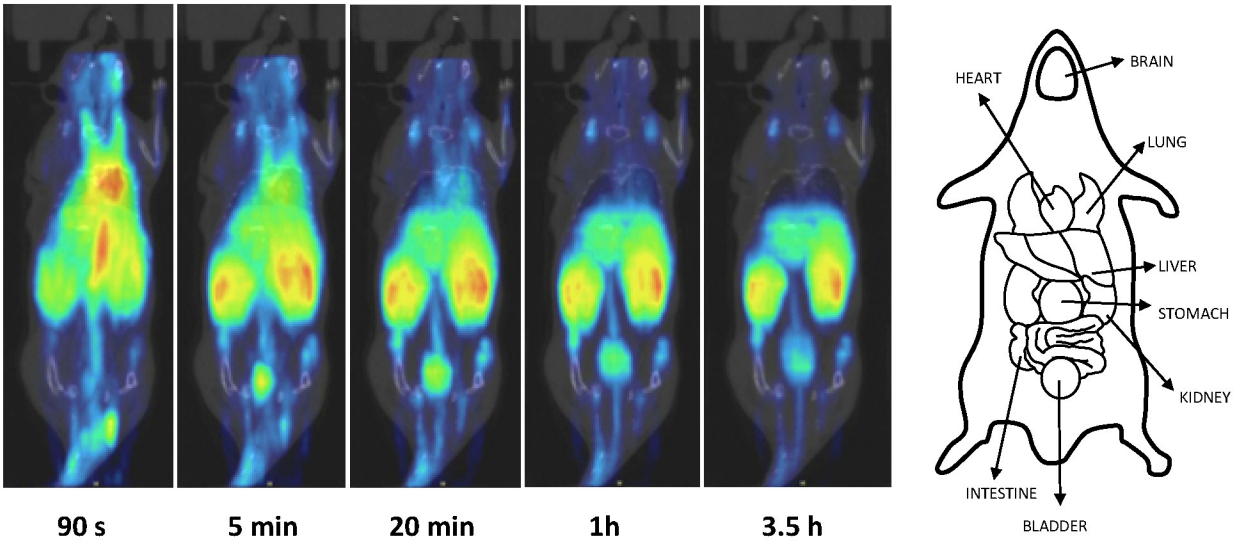

Figure 2. SPECT images of the biodistribution of iron oxide polymer nanoparticles in mice at different time points after tail vein injection.

View Article Online
DOI: 10.1039/C8NR03084G

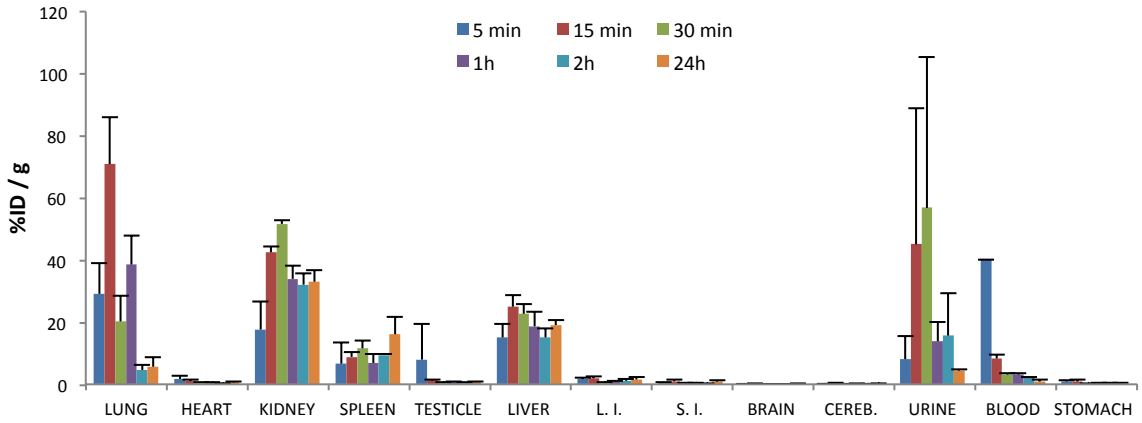

Figure 3. Accumulation of iron oxide polymer nanoparticles in various mice organs at different time points after tail vein injection, as determined by dissection and gamma counting. L.I.: Large intestine; S.I.: Small intestine; Cereb.: Cerebellum.

MR experiments.

Relaxometric measurements of indium-doped IONP suspensions for different dilutions are shown in Figure 7S. The r_2/r_1 ratio was 27.4 at 37 ºC for a frequency of 60 MHz, with an r2 = 38 $mFe^{-1}s^{-1}$ which is lower than what would correspond to a pure maghemite NPs of the same size due to the partial replacement of iron by a non magnetic ion. However, it still comparable to what has been reported for ultrasmall magnetic colloids,[43] thereby allowing the NPs to be detected by a standard T2-weighted MRI.

The biodistribution of IONPs was also followed by MRI in 6 mice. The results confirm those of gamma imaging and radiocounting. Figure 4A shows a clear reduction of the transverse relaxation times (T2) after injection of the IONPs, which mostly happens in the kidneys, thereby demonstrating the capacity of IONPs as negative MRI contrast agents for this organ. Conversely, no significant changes of the relaxation times were observed in the liver or spleen, thereby indicating a low retention of IONPs by the RES. The evolution of the change in T2 relaxation

View Article Online
DOI: 10.1039/C8NR03084G

times confirms that the accumulation of nanoparticles in the kidneys of mice takes place progressively during the first two hours after i.v. administration of the contrast agent (Figure 4B), which concurs with the SPECT and radiocounting results.

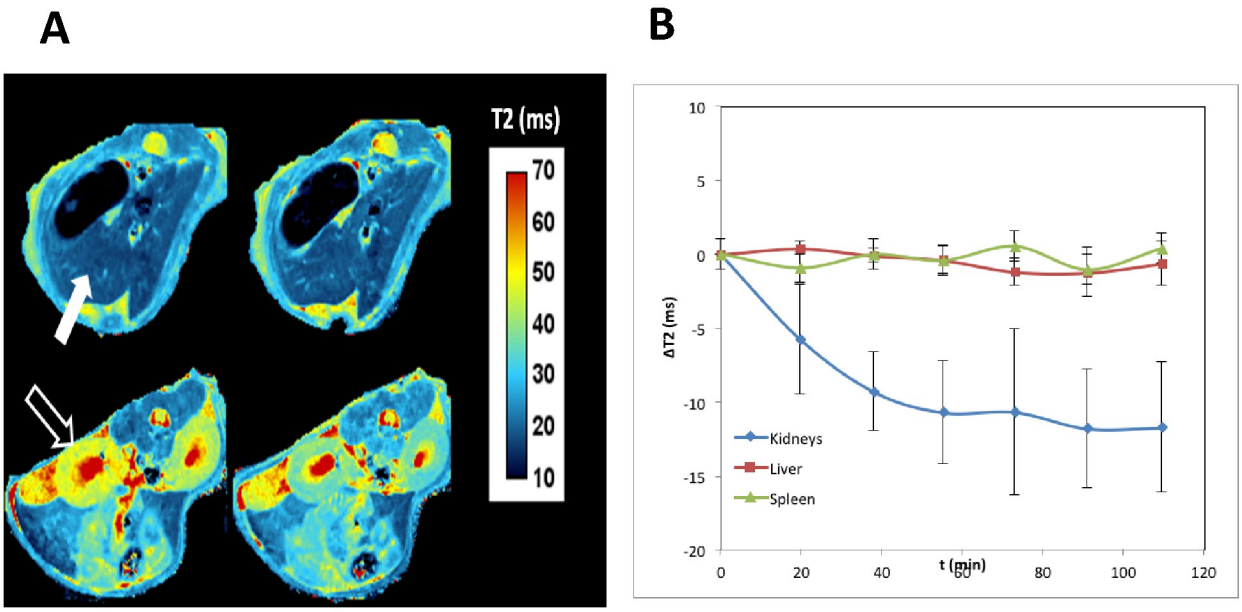

Figure 4. Figure caption. A: 2D-T2 relaxation maps at two different locations of the abdomen of a mouse, showing the liver (solid arrow, top images) and the kidneys (hollow arrow, bottom images) with the changes in T2 values before administration of the contrast agent (left) and 2 hours afterwards (right). B: average evolution of DT2 in the kidneys, liver, and spleen of 6 mice after injection of IONPs.

Histological studies.

A TEM histological inspection of kidney tissue slices shows the presence of iron oxide nanoparticles in samples from mice sacrificed at 0.5 h, 2 h, and 24 h after injection (Figure 5 and 4S-6S). Their presence was confirmed by EDX analysis and was scarce in all cases, although these nanoparticles were apparently more frequent in the 0.5 hour samples. IONPs were found inside proximal convoluted tubule cells, wherefore they had crossed the filtration membrane of the glomerulus before being reabsorbed by the proximal tubule cells. They were located inside

View Article Online
DOI: 10.1039/C8NR03084G

vesicles, probably lysosomes. The brightness in Figure 5 and 4S-6S corresponds to OsO_4, which was used as a staining agent and was adsorbed on the surface of the polymer coating, thus marking the contours of the whole IO-polymer composite nanoparticle. The sizes are actually within the range of a DLS hydrodynamic diameter distribution measured in vitro and are much larger than individual IONPs. EDX concentration profiles across the composite nanoparticles indicate the presence of iron in large areas within the composite nanoparticle. It can thus be inferred that the nanoparticles preserve the core-shell structure during the process, as from injection and through to tubule cell internalization, and consequently also when they cross the glomeruli, despite the fact that their hydrodynamic size is much larger than that of the glomerulus membrane pores. The fate of these nanoparticles is difficult to predict. They could be reabsorbed into the veins, they could be re-expelled into the tubules and be excreted through urine, or they could stay in the tubule cells until degradation by lysosomes.

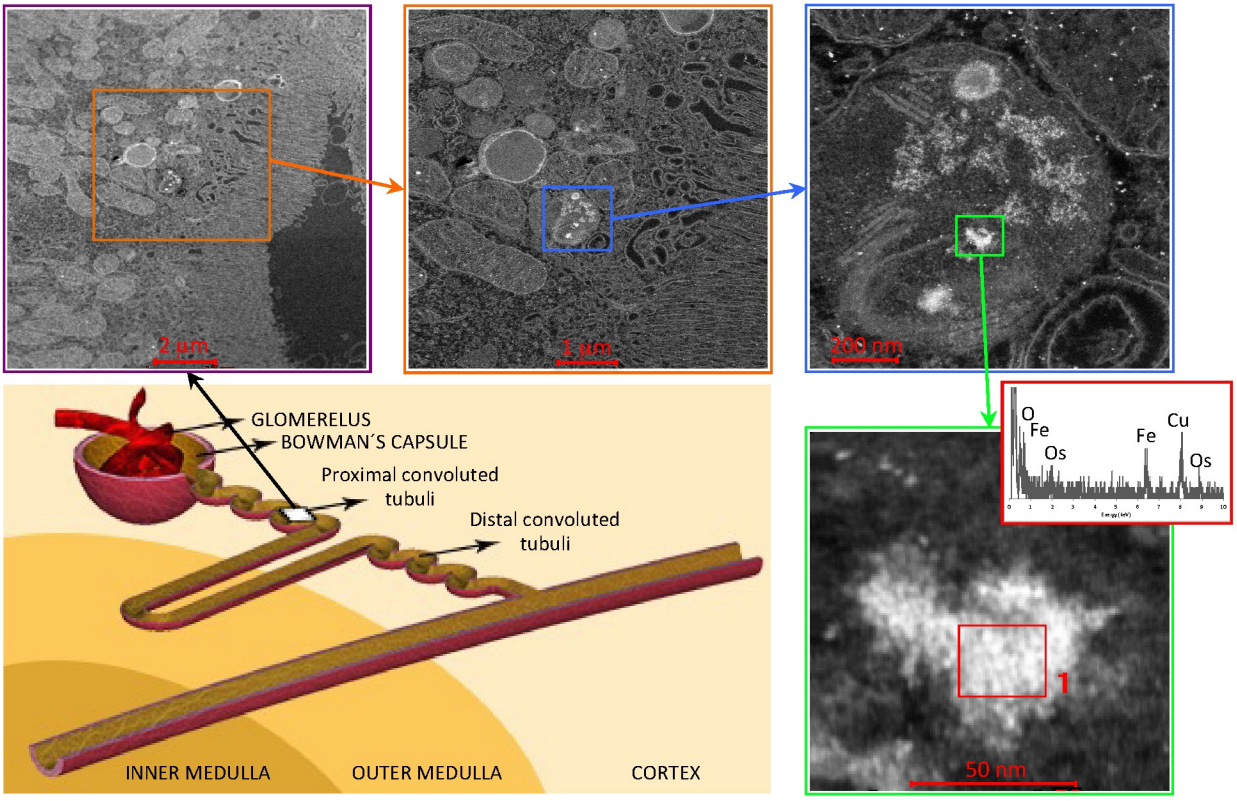

View Article Online
DOI: 10.1039/C8NR03084G

Figure 5. Figure caption. Dark field STEM images obtained with an HAADF detector, at different magnifications, of an iron oxide@P4VP@APEG nanoparticle in the proximal tubule cell of a kidney slice of a mouse sacrificed 30 minutes after injection. Uranyl and OsO_4 were used as staining agents. The drawing in the down left side of the figure shows the location of the nanoparticles within the kidney filtration system.

Comparison with previous studies

For the in vivo application of NPs, it is paramount to prevent NP retention by the RES before even considering targeted delivery to regions of interest. After this is ensured, it is then essential for NPs to be cleared rapidly from the body after accomplishing their function in order to reduce the risks of toxicity.[44] There are two pathways for excretion: renal and hepato-biliary clearance.[45] The hepato-biliary pathway goes from the liver into the small intestine and subsequently into fecal excretion. When NPs in the liver are trapped by hepatocytes, the transport thereof to feces is relatively fast.[46] The hepato-biliary clearance of NPs is inversely related to size, as it was observed in a study with gold NPs in a size range of 5 to 200 nm.[47] However, NPs are rarely taken up by endothelial cells and hepatocytes. They are mostly found in Kupffer cells,[45] where IONPs decompose into molecular iron species in a slow process and are finally incorporated into hemoglobin,[33] as it has been observed by ^{59}Fe direct-labeling of IONPs.

Liver fenestrae are relatively large (50-100 nm),[48] wherefore NPs with a wide ranges of sizes can circulate freely through the liver. Their retention in this organ is determined by recognition by macrophages, which partially depends on hydrodynamic size but mostly depends on the nanoparticle surface. For instance, QDs coated with mercaptopropionic acid and with very small sizes [D_p(TEM) = 3-4 nm, D_H(DLS) = 8.2 nm] showed higher accumulation in the liver and spleen (45 ID%/g) than in the kidneys (17 ID%),[49] as determined by chemical analysis. On the other hand, kidney fenestrae have an effective size cutoff of ≈ 10 nm,[50] and the upper size limit

View Article Online
DOI: 10.1039/C8NR03084G

of NPs for renal clearance is usually deemed to be approximately 6 nm.[51] For example, in a study of the biodistribution of cysteine-coated QDs with sizes of D_p (TEM) = 2.85, 3.02, 3.30, 3.80, 4.31 nm and D_H = 4.64, 4.91, 5.64, 6.40 nm, respectively, a cut-off size of 5.64 nm (DLS size) was established for renal excretion.[52] Similar results have been obtained with Au NPs.[33] These NPs can be produced with fine size control and can be directly labeled with ^{198}Au, which makes them ideal candidates for studying the filtering capacity of kidneys. It was observed in a series of Au NPs with core sizes of Dp = 1.4, 5, 18, 80, and 200 nm and hydrodynamic sizes D_H=2.9, 12.1, 21, 85, 205 nm[47] that only the smallest went through, although in amounts 10 times less than those found in the liver. Thus, a small size is necessary but does not guarantee the renal clearance of NPs, because they can still be strongly retained by the RES, depending on the coating. In that case, the coating was triphenylphosphine mono-sulfonate with a negative Zeta-potential. Other studies of Au NPs yielded similar results.[15] There are also exceptional cases in which a high accumulation in the kidneys has been found for nanoparticles with relatively large sizes. For example, naked Al_2O_3 NPs[34] with a size of 10 nm labeled internally with ^{13}N showed relatively high accumulation in the bladder (about 4% ID) and kidneys (about 1% ID) in comparison with the liver (about 4% ID). For larger nanoparticles (40 nm), the concentration in the bladder (2.6% ID) and kidneys (0.6% ID) was still high, despite a large increase in the liver (28% ID).

Indirect and direct biodistribution results for IONPs are summarized in tables 1 and 2, respectively. Most indirect labeling methods have shown a large accumulation in the liver and spleen and low excretion through urine.[53] Moreover, the supposed detection in the urinary system was attributed, at least in some cases, to detached free labels.[21,32,40,54] The few reports from direct radiolabeling studies indicate that IONPs are mostly retained in the liver and spleen

View Article Online
DOI: 10.1039/C8NR03084G

283 even for relatively small sizes (D_p = 2.2 nm, D_H = 20 nm) and after being coated with PEG[35] or
284 dextran.[36] These studies also show that the coating is decisive in IONP biodistribution. For
285 instance, IONPs with sizes of D_p = 4.8 nm and D_H =5.2 nm (therefore smaller than kidney
286 fenestrae) showed renal excretion by MRI only when they were coated with zwitterionic
287 molecules (dopamine sulfonate), but they were completely retained in the liver when the coating
288 was DMSA.[55]

Table 1. Biodistribution of iron oxides in mice by indirect labeling methods using radio-counting and radiocamera analysis.

Size (nm)		Coating	Radiolable		accumulation (%ID/g)					time	ref
D_p	D_H		radionuclide	ligand	liv.+spleen	kidney	blad.+urine	lung	other		
10	275	PLGA-GC [1]	99Tc	free (TcO_4^-)	41	< 1	4	13		2.2h	21
10	163	biotinated organosilica	99Tc	free (TcO_4^-)	12	0.8		2		3h	57 [2]
5	106	dextran	99Tc	DPA	99					10 min	58
	100	dextran	111In	ChL6-DOTA[3]	32	15		3		48h	59
8-12	95	PLGA-b-PEG-COOH	68Ga	NODA	4	0.5	< 0.2	0.5		2h	60
5	45	Aspartic	64Cu	DOTA	31	5				1h	61
5	40	dextran	99Tc	free (TcO_4^-)	24	1.8		0.7		2h	62
	30	dextran-PEG	19F-PEG		53.3 [4]	8.6 [4]	< 2	33.2 [4]		6h	20
	30	dextran	111In	ChL6-DOTA[3]	49	9		2		48h	59
	20	dextran	111In	ChL6-DOTA[3]	24	7		4		48h	59
5.5	23	PEG-BP	99Tc	DPA	11	2	14		5 [5]	2.2h	31
10	23	PAA	As*	free (AsO_4^{3-})	26		58			2h	55
10	23	PEG	As*	free (AsO_4^{3-})	25		12			2.5h	55
10	23	PAA-PEG	69Ge	Ge oxo-hydroxide	25		8			1h	63
10-15		DMSA	99Tc	free ion	2.6	0.35				1h	64
6.2	20	phospholipid-PEG	64Cu	DOTA	53	7		12	37 [6]	1h	32

[1] hydrophobic poly(D,L-lactic-co-glycolic acid) core and a hydrophilic glycol chitosan; [2] experiment performed in rats-rabbits; [3] ChL6: breast cancer targetting chimeric monoclonal antibody; [4]permeability Surface Area Product (PS/V) for Major Organs ($10^{-5}s^{-1}$); [5] heart and blood; [6] blood

View Article Online
DOI: 10.1039/C8NR03084G

Table 2. Biodistribution of iron oxides in mice by direct labeling methods

Method	Size (nm)		Coating	Radionucl.	accumulation (%ID/g)				time	ref
	D_p	D_H			liv.+spleen	kidney	blad.+urine	lungs		
radiocounting		80	AMI-25	59Fe	82	2		2	1h	33
radiocounting	7.8	37	PEG	111In	40				12h	35
PET/CT	2.2	20.6	dextran	68Ga	35	6	3		1h	36
magnetometer	9.2	110	DMSA		41			9	30 min	18

Low RES retention, urinary excretion, and the presence of the NPs in the kidneys are exceptional results compared to previous IONP biodistribution results. Actually, reports on semi-quantitative biodistribution analysis of dendronized IONPs by indirect IR luminescence labeling on the coating founded urinary excretion, but in combination with a rapid hepato-biliary clearance (which implies liver retention as explained in the introduction).[65] However, it must be stressed that radiolabeling by crystal doping with ^{111}In ions is direct, and therefore the radio signal unambiguously marks the position of IONPs until they are fully metabolized. MRI observations and histological studies confirm these results. The choice of ^{111}In as radio-label responds to its wide use in clinical practice that ensures a low toxicity. ^{111}In decays by electron capture (followed by gamma emission) leading ultimately to the formation of a cadmium atom (^{111}Cd), which of course has different chemical properties that may have an effect in the crystal structure of the NPs, by creating "local defects". However, the number of ^{111}In atoms introduced in the NPs is extremely low. This number can be calculated from the amount of radioactivity and the ^{111}In half-life as 2.1 x 10^{-11} mol/mCi. Hence, the formation of such defects due to spontaneous decay of ^{111}In is too low to enable its experimental characterization using, e.g., X-Ray diffraction.

View Article Online
DOI: 10.1039/C8NR03084G

The low retention in the liver and spleen can be explained by the stealth effect of PEG coatings due to their capacity to reduce protein adsorption and promote an adequate protein corona coating to avoid recognition by macrophages.[6] Indeed, numerous studies on PEG surface density have shown that grafted brush copolymers, such as that used in this report, allow a higher PEG density as compare to self-assembled linear chains.[66] It has also been shown that the capacity of PEG coating to avoid protein adsorption is directly related to the PEG grafting ratio.[66a] For instance, a PEG surface density of 30 ethyleneglycol monomers (EGM) per nm^2 was able to prevent protein adsorption, but when the density was decreased below 4 EG/nm^2 the anti-adsorption effect was negligible. In our case, NMR studies have shown that the APEG grafting reaction on P4VP backbone chains has a nearly 100% yield (see SI file). Thus, considering the nucleus average diameter of 11.5 nm obtained from TEM images the PEG density in our nanoparticles would be 234 EGM/nm^2 (Even considering the external nanoparticle diameter of 18 nm from DLS, the density (96 EGM/nm^2) would be still high in comparison with the cited report).

A second significant finding in this study was that our MNPs showed a certain accumulation in the kidneys that is sufficient to provide a clear MRI negative contrast of this organ. Gd complexes are the preferred MRI contrast agents in clinical practice because they give a bright contrast, whereas IONPs have an image darkening effect.[67a] On the other hand, IONPs are advantageous in terms of blood circulation times (which reduces their targetting efficiency), detection sensitivity, and multimodal-imaging.[67b] Besides, IONPs can be especially indicated for patients with liver and kidney problems, because Gd complexes present toxicity effects in these patients.[67c] However, up to now their use has been restricted to liver. This report opens the way for their clinical use in kidneys also.

View Article Online
DOI: 10.1039/C8NR03084G

Presence in the urine and in the kidney tubule cells means that NPs can cross the glomerular barrier. It is surprising that NPs such as those used in these experiments, consisting of multicore composite nanoparticles containing several individual IONPs with a hydrodynamic size of approximately 20 nm, could be filtered through the glomeruli pores that are approximately one-third the size. Nevertheless, this was corroborated by TEM observations, which showed the presence of the composite nanoparticles in the interior of proximal tubule cells. It has to be pointed out that cut-off sizes of 5-6 nm for kidney filtration had been determined with rigid inorganic NP systems.[33,52] Our system has a distinct arquitecture: 1) the individual iron oxide nanoparticles in the multicore nucleus are not bonded to each other, but they are loosely packed within the polymer matrix; 2) the polymer coating is formed y hydrophilic PEG chains. Therefore we may expect some degree of flexibility in our NPs that could allow them to squeeze through the pores of the glomeruli similarly to how red blood cells pass through capillaries in the circulatory system.

Experimental

Materials. Iron(III) bromide ($FeBr_3$, 98%), Iron(II) bromide ($FeBr_2$, 98%), poly(4-vinyl pyridine) (P4VP, Mn ≈ 60.000 Da) were all products of Sigma Aldrich and were used as received without further purification. Poly(ethylene glycol) (200) acrylate (APEG(200), Mn(PEG) = 200 Da, Monomer&Polymer), and poly(ethylene glycol) (1000) monoacrylate (APEG(1000), Mn(PEG) = 1000 Da, Monomer&Polymer) were purified by a modified method.[9] Carboxylic acid terminated APEG(1000), APEG(1000)COOH, was prepared by reacting succinic anhydride with the hydroxyl end group of APEG(1000) following the procedure described elsewhere.[42] The purity of polyethylene glycol derivatives was confirmed by proton

View Article Online
DOI: 10.1039/C8NR03084G

NMR spectroscopy (BRUKER AV-400) and mass spectroscopy (MALDI TOF-MS, BrukerMicroFlex).

Synthesis of core-shell IONPs. The preparation of the ferrofluids was performed in two steps: 1) synthesis of maghemite/P4VP nanocomposites, and 2) PEG coating of the nanocomposite NPs in a PBS medium.

Maghemite/P4VP nanocomposites were prepared by in situ precipitation in films of iron–P4VP coordination compounds, following the procedure described elsewhere.[8] A stock solution of iron and P4VP was prepared by dissolving 0.1 g of P4VP (952 μmol in monomer), 0.4 mL of $FeBr_3$ 1M (400 μmol), 0.2 mL of $FeBr_2$ 1M (200 μmol) in 5 mL of 0.01 M HBr. A vial of 0.5 mL of 5 mCi $^{111}InCl_3$ and another vial of 0.5 mL of 3 mCi $^{111}InCl_3$ were mixed, and 117 μL of the P4VP-iron stock solution was added to this mixture, and then it was evaporated in a Petri dish to obtain a film. The film was treated with 1 M NaOH solution for 1 h and washed with water to obtain a maghemite nanocomposite. This nanocomposite was dispersed in 2 mL of HCl 11mM for a final pH=3.0. Separately, 1.9 mL of stock solution of PEG acrylate polymers mixture was prepared by dissolving 90 μL of APEG(200) and 10 μg of APEG(1000)COOH in water. 44,3 μL of this solution was added to the nanoparticle suspension and allowed to react for 20 h under magnetic stirring at 70 ^{o}C. After cooling, the pH of the suspension was adjusted to neutral by addition of a sodium bicarbonate solution, the volume was adjusted to 3 mL, and the solution was filtered through a sterile 0.22 μm membrane filter (Millipore). The resulting IONP suspension was used in radiocounting biodistribution experiments. The final composition of the suspension is presented in Table 3.

Table 3. Composition of injected fluid

View Article Online
DOI: 10.1039/C8NR03084G

	mg/mL	μM	Molar ratio*
Fe_2O_3	0.17	2.30	1
4VP monomer	0.35	3.27	1.4
EG monomer	0.35	6.46	2.8
^{111}In			10^{-4}

* In the case of Fe2O3 the value corresponds to Fe moles

An scheme the P4VP-APEG brush copolymer structure is shown in the SI file.

The NP suspension for the in vivo SPECT experiment was prepared in the same way as in the radiocounting experiments except that the amount of radiotracer was 3 vials of 5mCi $^{111}InCl_3$, and the amounts of the rest of components were adjusted for a 150 μL final volume.

For the leaching experiments, relaxometry measurements, histologic examination and TEM characterization, a nanoparticle suspension was prepared in the same way as above except that the $InCl_3$ was non-radioactive in this case.

For the x-ray powder diffraction studies of Fe-In crystalline miscibility, 4 polymer-nanoparticle samples were also prepared in a similar way except that the amounts of reactants was 10 times higher and the In/Fe atomic ratio was 1/4000, 1/100, 1/10, and 1/1, respectively. Pure iron/indium oxide samples were prepared by precipitation in water in the absence of polymer, and then the samples were also submitted to heat treatment at 70 ^{o}C during 20h as for composite samples.

Sample characterization. The total iron content in the IONP samples has been determined by atomic absorption in a plasma 40 ICP Perkin–Elmer spectrometer. The size of the maghemite nanoparticles was determined by transmission electron microscopy (TEM) images in a Philips CM30 microscope. STEM dark field images have been acquired with a HAADF detector (Fischione) that only captures strongly scattered electrons in order to get a compositional image

View Article Online
DOI: 10.1039/C8NR03084G

of the sample. The hydrodynamic size distribution of the dispersed nanoparticles in the ferrofluids was determined by Dynamic Light Scattering (DLS) using the Zetasizer Nano ZS of Malvern Panalytical that uses a 175^{o} detection angle with respect to the incident beam. The suspensions were measured as prepared, without dilution (conc.: 0.17 mg(Fe_2O_3)/mL, pH=7.4). X-rays diffraction experiments were performed in a Rigaku D max B apparatus.

SPECT and radiocounting measurements. All the animal procedures were performed in accordance with the Spanish policy for animal protection (RD53/2013), which meets the requirements of the European Union directive 2010/63/UE regarding the protection of animals used in experimental procedures. The guidelines were approved by the Ethical Committee of CIC biomaGUNE and authorized by the regional government. Mice (BALB/cJRJ, 8-12 weeks of age, Janvier Labs, France), were housed in a controlled environment (12:12 light/dark cycle with dawn and dusk transitional periods, room temperature 22 °C, and 55% relative humidity) and maintained on commercially available pelleted diet and sterilized water *ad libitum*. Three animals per labeled species were used for *in vivo* SPECT/CT experiments; dissection and gamma counting experiments were performed on three animals at each time point.

SPECT/CT images: SPECT/CT images were acquired using the eXplore speCZT CT preclinical imaging system (GE Healthcare, Little Chalfont, UK). With the mouse under isoflurane anesthesia (1.5-2% in oxygen), whole-body dynamic SPECT/CT scans were acquired immediately after injection in an energy window of 100-200 keV. During image acquisition, mice were kept normothermic using a heating blanket (Homeothermic Blanket Control Unit; Bruker BioSpin GmbH, Karlsruhe, Germany). After each SPECT scan, CT acquisitions were performed to provide anatomical information about each animal. The CT acquisition consisted

View Article Online
DOI: 10.1039/C8NR03084G

of 220 views acquired in 0.88° increments around the animal with 16 ms exposure per view. The X-ray tube settings were 70 kV and 32 mA.

The SPECT images were reconstructed using the 2D OSEM iterative algorithm with 10 iterations/1 subsets in the 154-188 keV energy window. The images were reconstructed into 128 x 128 x 32 arrays with a voxel size of 0.4 x 0.4 x 2.46 mm and were corrected for scatter but not attenuation. The CT images were reconstructed using a cone beam filtered back-projection Feldkamp algorithm into 437 x 437 x 523 arrays with a voxel size of 0.2x 0.2 x 0.2 mm.

Dissection and gamma counting: Animals (n = 18, three per time point) were anesthetized with isofluorane and a solution of labeled iron oxide@P4VP@APEG composite nanoparticles were injected through the tail vein. After injections, animals were allowed to recover. Just before sacrifice by cervical dislocation (five, 15 and 30 min and one, 2, and 24 h after dose administration), animals were anaesthetized again and blood samples collected by cardiac puncture. After sacrifice, liver, lungs, brain, cerebellum, intestine, and thyroid glands were quickly removed and rinsed twice with deionised water; urine samples were also obtained. The amount of radioactivity in each organ was determined using an automatic gamma counter.

Minispec and Magnetic Resonance Imaging (MRI) measurements. Relaxivities were measured at 37 °C on a Bruker Minispec MQ60 instrument (Bruker Biospin GmbH, Ettlingen, Germany) operating at 1.47 T (60 Mhz). All experiments were performed using a volume of 300µl of a dispersion of the ferrofluid in water up to 0.1mM iron concentration. Longitudinal (T1) and transverse (T2) relaxation times were determined using the inversion recovery and the CPMG methods, respectively. T1 and T2 relaxation times allowed us to determine the corresponding relaxivities (r1 and r2) fitting the relaxation rate (R1 and R2) dependence of the concentration using the following equation:

View Article Online
DOI: 10.1039/C8NR03084G

$$R_{1,2}(s^{-1}) = \frac{1000}{T_{1,2}\ (ms)}$$

437

$$R_{1,2}(s^{-1}) = R_{10,20} + r_{1,2}\ [CA]$$

438

439 where $R_{10,20}$ corresponds to the relaxation rates of the solvent used to prepare the solutions, [CA]
440 is the concentration of the contrast agent, and $r_{1,2}$ is the relaxivity.
441 MRI studies have been performed on a 7 T on horizontal bore Bruker biospec USR 70/30 MRI
442 system (Bruker Biospin, Ettlingen, Germany) using the BGA12-S mini imaging gradient and a
443 40 mm inner diameter volume-coil working in quadrature for both, signal transmission and
444 reception. A number of n=6 BALB/cJRj female mice (8 weeks old) weighing (22.7±2.1 g) were
445 included in the study. Animals were anesthetized with isofluorane (2-3 % carried in a 35/65
446 O_2/N_2 gas mixture) and temperature was maintained at 37±1 ºC with a water pad. Temperature
447 and respiration rate were continuously monitored inside the MRI using a SAII M1030 system,
448 used also for synchronize image acquisition with the respiration rate of the animal.
449 Using a PE catheter and a 30G needle attached to the tail vein of the animals, 100 µl of contrast
450 agent (200 µg/ml of Iron in NaCl 0.007 M and pH 7.5) was injected to the animals inside the
451 magnet, allowing the acquisition of MR images prior, and up to 240 min post injection, in
452 intervals of 20 min. A multi-slice multi-echo pulse sequence (20 echoes, TE=8 ms; TR=2500
453 ms; Averages, Nav=2; Matrix = 160x160 points; FOV = 24x24 mm; spatial resolution =
454 150x150 um; 8-12 slices of 1 mm thickness in 2 slice packages (one covering the kidneys/spleen
455 region and another the liver region)). T2 parametric maps were generated on a pixel-by-pixel
456 basis fitting the acquired images to a 2 parameter exponential decay (y=a+b*exp(-TE/T2)) using
457 self-developed routines for the NIH software Image-J. Mean differences in T2 relaxation times

View Article Online
DOI: 10.1039/C8NR03084G

($\Delta T2 = T2_t - T2_{pre\ contrast}$) were calculated for each time-point (t) in manually selected regions of interest (ROIs: liver, Spleen, Kidney).

Conclusions

This report presents SPECT and gamma-counting biodistribution studies using a new, reliable, and direct radiolabeling method, which is complemented by an MRI biodistribution study that is also direct. The results obtained using densely PEG-coated IONPs are outstanding. Both gamma and MRI studies revealed a low presence in the liver and spleen, which is clear evidence that NPs have successfully avoided the effects of the RES and that they are good candidates for targeted therapy after being functionalized with a targetting agent. Furthermore, gamma-labeling studies showed considerable excretion in the urine, which substantially reduces the problem of eliminating NPs after being used in therapeutic applications. Another notable and surprising result is that IONPs, which have a hydrodynamic size that is three times as large as kidney fenestrae, can cross the glomeruli and be mostly excreted through the urine. However, the most evident and immediate clinical application of NPs presented in this report is their efficiency as an MRI contrast agent for kidneys, which is a field that has been scarcely explored. The biodistribution and physical properties of the hybrid, radioactive, and magnetic tracer that we have presented will allow it to be used for targeting and used as a contrast agent for MRI and SPECT outside the liver.

Conflicts of interest

There are no conflicts to declare.

Author contributions

View Article Online
DOI: 10.1039/C8NR03084G

V. Gómez-Vallejo, has participated in the planning, realization and data analysis of SPECT and gamma counting experiments, M. Puigivila has participated in the realization of the animal handling and gamma counting experiments, S. Plaza-García has participated in the realization of the MRI experiments, B. Szczupak has participated in the realization of the SPECT experiments, R. Piñol has participated in the synthesis and characterization of the nanoparticle samples, and in the writing of the experimental section of the manuscript, J.L. Murillo and G. Lou have participated in the synthesis and characterization of the nanoparticle samples, V. Sorribas has realized the histology experiments, S. Veintemillas, has participated in the relaxometry experiments and the writing of the manuscript, P. Ramos-Cabrer has participated in the planning and realization of the MRI experiments and in the writing of the manuscript, Jordi Llop has participated in the ,planning, realization and interpretation of the data of the SPECT and gamma counting experiments and in the writing of the manuscript, A. Millán has participated in the planning of the experiments, synthesis of the radiolabeled nanoparticles, TEM characterization of nanoparticles and tissues, interpretation of the data and in the writing of the manuscript.

Acknowledgments

Financial support by the Spanish Ministry of Science and Innovation (MAT2014-52069-R) (SAF2014-53413-R) (PC2015-1-05 53-80) is gratefully acknowledged. The authors would like to acknowledge the use of Laboratory of Advanced Microscopy-LMA, and the Servicio General de Apoyo a la Investigación-SAI, Universidad de Zaragoza.

View Article Online
DOI: 10.1039/C8NR03084G

References

1 a) W. H. De Jong and P. J. A. Borm, *Int. J. Nanomed.* 2008, **3**, 133; b) S. Parveen, R. Misra, S. K. Sahoo, *Nanomedicine* 2012, **8**, 147.

2 F. Kiessling, M. E.Mertens, J. Grimm and T. Lammers, *Radiology* 2014, **273**, 10.

3 L. Liao, J. Liu, E. C. Dreaden, S. W. Morton, K. E Shopsowitz,. P.T. Hammond and J. A. Johnson, *J. Am. Chem. Soc.* 2014, 136, 5896.

4 D. E. Owens III and N. A. Peppas, *Int. J. Pharm.* 2006, **307**, 93.

5 F. Alexis, E. Pridgen, L. K. Molnar and O. C. Farokhzad, *Mol. Pharm.* 2008, 5, 505.

6 S. Schöttler, G. Becker, S. Winzen, T. Steinbach, K. Mohr, K. Landfester, V. Mailänder and F. R. Wurm, *Nat. Nanotechnol.* 2016, **11**, 372.

7 J. Lipka, M. Semmler-Behnke, R. A. Sperling, A. Wenk, S. Takenaka, C. Schleh, T. Kissel, W. J. Parak and W. G. Kreyling *Biomaterials* 2010, **31**, 6574.

8 L. M. A. Ali, M. Gutiérrez, R. Cornudella, J. A. Moreno, R. Piñol, L. Gabilondo, A. Millán and F. Palacio, *J. Biomed. Nanotechnol.* 2013, **9**, 1272.

9 L. M. A. Ali, R. Piñol, R. Villa-Bellosta, L. Gabilondo, A. Millán, F. Palacio and V. Sorribas, *Toxicol. In Vitro*, 2015, **29**, 962.

10 R. Piñol, C. D. Brites, R. Bustamante, A. Martínez, N. J. O. Silva, J. L. Murillo, R. Cases, J. Carrey, C. Estepa, C. Sosa, F. Palacio, L. D. Carlos and A. Millán, *ACS Nano* 2015, *9*, 3134.

11 H. Ding and F. Wu, *Theranostics* 2012, *2*, 1040.

12 G. P. Luke, J. N. Myers, S. Y. Emelianov and K. V. Sokolov, *Cancer Res.* 2014, **74**, 5397.

13 B. Chertok, A. J. Cole, A. E. David and V. C. Yang, *Mol. Pharm.* 2010, *7*, 375.

14 T. F. Massoud and S. S. Gambhir, *Genes Dev.* 2003, **17**, 545.

View Article Online
DOI: 10.1039/C8NR03084G

15 W. H. De Jong, W. I. Hagens, P. Krystek, M. C. Burger, A. J. A. M. Sips and R. E. Geertsma, *Biomaterials* 2008, **29**, 1912.

16 L. Liu, T. K. Hitchens, Q. Ye, Y. Wu, B. Barbe, D. E. Prior, W. F. Li, F. C. Yeh, L. M. Foley, D. J. Bain and C. Ho, *Biochim. Biophys. Acta* 201**3**, **1830**, 3447.

17 T. K. Jain, M. K. Reddy, M. A. Morales, D. L Leslie-Pelecky and V. Labhasetwar, *Mol. Pharm.* 2013, *5*, 316.

18 L. Gutiérrez , R. Mejías , F. J. Lázaro , C. J. Serna D. F. Barber and M. P. Morales, *IEEE Trans. Magn.* 2013, **49**, 398.

19 H. Amiri,. R. Bustamante, A. Millán, N. J.O. Silva, R. Piñol, L. Gabilondo, F. Palacio, P. Arosio, M. Corti and A. Lascialfari, *Magn. Reson. Med.* 2011, **66**, 1715.

20 N. K. Devaraj, E. J. Keliher, G. M.Thurber, M. Nahrendorf and R. Weissleder, *Bioconjug Chem.* 2009, **20**, 397.

21 P. W. Lee, S. H. Hsu, J. J. Wang, J. S. Tsai, K. J. Lin, S. P. Wey, F. R. Chen, C. H. Lai, T. C. Yen and H. W. Sung, *Biomaterials* 2010, **31**, 1316.

22 A. P. Khandhar, R. M. Ferguson, H. Arami and K. M. Krishnan, Biomaterials, 2013, **34**, 3837.

23 M. Fani, J. P. André, and H. R. Maecke, *Contrast Media Mol. Imaging* 2008, **3**, 53.

24 J. Llop, V. Gomez-Vallejo and P. N. Gibson, *Isotopes in Nanoparticles: Fundamentals and Applications*, CRC Press, Boca Raton, 2016.

25 F. Chen, P. A. Ellison, C. M. Lewis, H. Hong, Y. Zhang, S. Shi, R. Hernandez, M. E. Meyerand, T. E. Barnhart and W. Cai, *Angew. Chem. Int. Ed.* 2013, **52**, 13319.

26 D. Psimadas, P. Georgoulias, V. Valotassiou and G. Loudos, *J. Pharm. Sci.* 2012, **101**, 2271.

View Article Online
DOI: 10.1039/C8NR03084G

27 a) A. Helbok, C. Decristoforo, G. Dobrozemsky, C. Rangger, E. Diederen, B. Stark, R. Prassl and E. vonGuggenberg, *J. Liposome Res.* 2011, *20*, 219; b) A. L. Petersen, A. E. Hansen, A. Gabizon, T. L. Andresen, *Adv. Drug Deliv. Rev.* 2012, **64**, 1417.

28 S. J. Kennel, J. D. Woodward, A. J. Rondinone, J. Walla, Y. Huang and S. Mirzadeh, *Nucl. Med. Biol.* 2008, **35**, 501.

29 M. Schottelius, B. Laufer, H. Kessler and H. J. Wester, *Acc. Chem. Res.* 2009, **42**, 969.

30 S. Kommareddy and M. Amiji, *J. Pharm. Sci.* 2007, **96**, 397-407.

31 L. Sandiford, A. Phinikaridou, A. Protti, L. K. Meszaros, X. Cui, Y. Yan, G. Frodsham, P. A. Williamson, N. Gaddum, R. M. Botnar, P. J. Blower, M. A. Green and R. T. M. de Rosales, *ACS Nano* 2013, **7**, 500.

32 C. Glaus, R. Rossin, . J. Welch and G. MBao, In Vivo Evaluation of ^{64}Cu-Labeled *Bioconjugate Chem.* 2010, **21**, 715.

33 R. Weissleder, D. D. Stark, B. L. Engelstad, B. A. Bacon, C. C. Compton, D. L. White, P. Jacobs and J. Lewis, *AJR Am. J. Roentgenol.* 1989, **152**, 167.

34 C. Pérez-Campaña, V. Gómez-Vallejo, M. Puigivila, A. Martín, T. Calvo-Fernández, S. E. Moya, R. F. Ziolo, T. Reese and J. Llop, *ACS Nano* 2013, **7**, 3498.

35 J. Zeng, B. Jia, R. Qiao, C. Wang, L. Jing, F. Wang and M. Gao, *Chem. Commun.* 2014, **50**, 2170.

36 J. Pellico, J. Ruiz-Cabello, M. Saiz-Alía, G. del Rosario, S. Caja, M. Montoya, L. Fernández de Manuel, M. P. Morales, L. Gutiérrez, B. Galiana, J. A. Enríquez and F. Herranz *Contrast Media Mol. Imaging* 2016, **11**, 203.

37 K. Stojanov, I. S. Zuhorn, R. A. Dierckx and E. F. de Vries, *Pharm. Res.* 2012, **29**, 3213.

View Article Online
DOI: 10.1039/C8NR03084G

38 R. R. Patil, J. Yu, S. R Banerjee, Y. Ren, D. Leong, X. Jiang, M. Pomper, B. Tsui, D. L Kraitchman and H. Q. Mao, *Mol. Ther.* 2011, **19**, 1626.

39 H. Lee, B. Hoang, H. Fonge, R. M. Reilly and C. Allen, *Pharm. Res.* 2010, **27**, 2343.

40 M. P. Melancon, W. Lu, Z. Yang, R. Zhang, Z. Cheng, A. M. Elliot, J. Stafford, T. Olson, J. Z. Zhang and C. Li, *Mol. Cancer Ther.* 2008, **7**, 1730.

41 S. J. DeNardo, G. L. DeNardo, A. Natarajan, L. A. Miers, A. R. Foreman, C. Gruettner, G. N. Adamson and R. Ivkov, *J. Nucl. Med.* 2007, **48**, 437.

42 M. Wagner, S. Wagner, J. Schnorr, E. Schellenberger, D. Kivelitz, L. Krug, M. Dewey, M. Laule, B. Hamm and M. Taupitz, *J. Magn. Reson. Imaging* 2011, **34**, 816.

43 C. Corot, P. Robert, J. M. Idée and M. Port, *Adv. Drug Deliv. Rev.* 2006, **58**, 1471.

44 A. J. Cole, V. C. Yang and A. E. David, *Trend Biotechnol.* 2011, **29**, 323.

45 E. Sadauskas, H. Wallin, W. Stoltenberg, U. Vogel, P. Doering, A. Larsen and G. Danscher, *Part. Fibre Toxicol.* 2007, **4**, 10.

46 G. Renaud, R. L. Hamilton and R. J. Havel, *Hepatology* 1989, **9**, 380.

47 S. Hirn, M. Semmler-Behnke, C. Schleh, A. Wenk, J. Lipka, M. Schäffler, S. Takenaka, W. Möller, G. Schmid, U. Simon and W. G. Kreyling, *Eur. J. Pharm. Biopharm.* 2011, **77**, 407.

48 F. Braet, E. Wisse, P. Bomans, P. Frederik, W. Geerts, A. Koster, L. Soon and S. Ringer, *Microsc. Res. Tech.* 2007, **70**, 230.

49 J. Gao, K. Chen, R. Xie, S. Lee, Z. Cheng, X. Peng and X. Chen, *Small* 2010, **6**, 256.

50 J. E. Zuckerman, C. H. J. Choi, H. Han and M. E. Davis, *PNAS* 2012, **109**, 3135.

51 M. Longmire, P. L. Choyke and H. Kobayashi, *Nanomedicine* 2008, **3**, 703.

View Article Online
DOI: 10.1039/C8NR03084G

52 H. S. Choi, W. Liu, P. Misra, E. Tanaka, J. P. Zimmer, B. I. Ipe, M. G. Bawendi and J. V. Frangioni, *Nat. Biotechnol.* 2007, **10**, 1165.

53 H. Arami, A. Khandhar, D. Liggitt and K. M. Krishnan, *Chem. Soc. Rev.* 2015, **44**, 8576.

54 F. Chen, P. A. Ellison, C. M. Lewis, H. Hong, Y. Zhang, S. Shi, R. Hernandez, M. E. Meyerand, T. E. Barnhart and W. Cai, *Angew. Chem. Int. Ed.* 2013, **52**, 13319 .

55 Z. Zhou, L. Wang, X. Chi, J. Bao, L. Yang, W. Zhao, Z. Chen, X. Wang, X. Chen and J. Gao, *ACS Nano* 2013, **7**, 287.

56 R. P. Chauhan, R. Mathur , G. Singh, N. Bag, S. Singh, K. Chuttani, B. S. H. Kumar, S. K. Agrawal and A. K. Mishra, *J. Mater. Sci.* 2013, **48**, 3913.

57 R. Torres Martin de Rosales, R. Tavaré, A. Glaria, G. Varma, A. Protti and P. J. Blower, *Bioconjugate Chem.* 2011, **22**, 455.

58 A. Natarajan, C. Gruettner, R. Ivkov, G. L. DeNardo, G. Mirick, A. Yuan, A. Foreman and S. J. DeNardo, *Bioconjugate Chem.* 2008, **19**, 1211.

59 E. Locatelli, L. Gil, L. L. Israel, L. Passoni, M. Naddaka, A. Pucci, T. Reese, V. Gomez-Vallejo, P. Milani, M. Matteoli, J. Llop, J. P. Lellouche and M. C. Franchini *Int. J. Nanomed.* 2012, **7**, 6021.

60 H. Y. Lee, Z. Li, K. Chen, A. R. Hsu, C. Xu, J. Xie, S. Sun and X. Chen, *J. Nucl. Med.* 2008, **49**, 1371.

61 S. Shanehsazzadeh, M. A. Oghabian, F. J. Daha, M. Amanlou and B. J. Allen, *J. Radioanal. Nucl. Chem.* 2013, **295**, 1517.

62 R. Chakravarty, H. F. Valdovinos, F. Chen, C. M. Lewis, P. A. Ellison, H. Luo, M. E. Meyerand, R. J. Nickles and W. Cai, *Adv. Mater.* 2014, **26**, 5119.

View Article Online
DOI: 10.1039/C8NR03084G

63 S. Fatahian, D. Shahbazi-Gahrouei, M. Pouladian, M. H. Yousefi, Gh. R. Amiri and A. Noori, *J. Radioanal. Nucl. Chem.* 2012, **293**, 915.

64 Z. Yang, W. Zang, J. Zou and W. Shi, *Polymer* 2007, **48**, 931.

65 a) C. Ghobril, G. Popa, A. Parat, Billotey, Taleb, P. Bonazza, S. Begin-Colin, D. Felder-Flesch, *Chem. Commun.*, 2013, **49**, 9158; b) A. Walter, A. Garofalo, P. Bonazza, F. Meyer, H. Martinez, S. Fleutot, C. Billotey, J. Taleb, D. Felder-Flesch, S. Begin-Colin, *ChemPlusChem* 2017, **82**, 647.

66 a) S. Pasche, S. M. De Paul, J. Vörös, N. D. Spencer, M. Textor, *Langmuir* 2003, **19**, 9216; b) G. Emilsson, R. L. Schoch, L Feuz, F Höök, R Y. H. Lim, A B. Dahlin, *ACS Appl. Mater. Interfaces* 2015, **7**, 7505; c) F. Zhou, W. T. S. Huck, *Phys. Chem. Chem. Phys.* 2006, **8**, 3815; d) W. Senaratne, L. Andruzzi, and C. K. Ober, *Biomacromolecules* 2005, **6**, 2427; e) O.Azzaroni, I. Szleifer (Eds) *Polymer and Biopolymer Brushes: for Materials Science and Biotechnology*, Wiley, 2018.

67 a) Y. Okuhata, *Adv. Drug Delivery Rev.*, 1999, **37**, 121; b) Z. R. Stephen, F.M. Kievit, M. Zhang, *Materials Today*, 2011, **14**, 330; c) M. Rogosnitzky and S. Branch, *BioMetals*, 2016, **29**, 365.

View Article Online
DOI: 10.1039/C8NR03084G

Table of contents

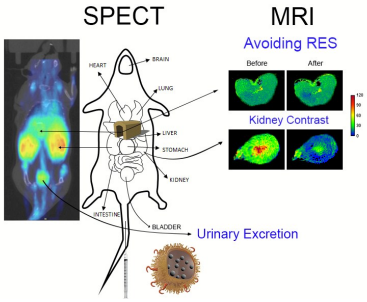

PEG coated magnetic nanocarriers avoid ReticuloEndothelialSystem, and give MRI contrast in kidneys. Results are supported by SPECT, gamma-counting, MRI and TEM histology.